DOI: 10.13009/EUCASS2023-535
Aerospace Europe Conference 2023 – 10TH EUCASS – 9TH CEAS

Kākāpō - An Experimental Test Facility for the Performance Analysis of Heaterless Hollow Cathodes at High Applied Magnetic Field Strengths

Jakob Balkenhohl⋆†*, Nicholas Rattenbury*⋆ *and John Cater*⋆⋆
⋆ *Te Pūnaha Ātea - Auckland Space Institute, The University of Auckland, Auckland, 1010, Aotearoa New Zealand*
⋆⋆ *University of Canterbury, Christchurch, 8041, Aotearoa New Zealand*
jakob.balkenhohl@auckland.ac.nz · n.rattenbury@auckland.ac.nz · john.cater@canterbury.ac.nz
†Corresponding author

Abstract

As part of the development of a low-power applied-field magnetoplasmadynamic thruster (AF-MPDT) in New Zealand, an experimental test facility has been designed and commissioned at the Te Pūnaha Ātea Space Institute in Auckland for the performance analysis of thermionic emission hollow cathodes at high applied axial magnetic field strengths. This work gives an overview of this apparatus and its different subsystems. The design and development of the magnet and plasma diagnostics subsystems are discussed in greater detail. Finally, the results of first cathode plasma discharge tests as well as future test plans are presented.

1. Introduction

A steady increase in demand for cheaper and more efficient space access is driving development in electric space propulsion. Concurrently, as high-temperature superconductors (HTS) and miniaturised cryocooler technologies mature, their potential to be applied to space technology is also growing. This has renewed interest in applied-field magnetoplasmadynamic (AF-MPD) thrusters, which have been an infeasible option for space applications so far due to their high power demands and could benefit from greater magnetic field strengths.[6] A research group in New Zealand funded by the New Zealand Ministry of Business, Innovation and Employment aims to design and build an HTS-AF-MPD thruster at low power levels for satellite propulsion. Power levels below 10 kW and applied magnetic field strengths from 500 mT to 1 T are targeted within this project's scope.

A challenge associated with a more novel low-power MPD operating regime is that the more commonly used rod cathodes, in combination with the propellant being injected into the backplate of the anode, do not allow for sufficient ionisation and plasma formation at low currents. Thermionic emission hollow cathodes (HCs) have a long history of being used as an electron source to neutralise plasma plumes in hall-effect thrusters and ion thrusters with plenty of space flight heritage.[8] The technology has matured significantly since their invention in the late 1960s,[11] and the range of applications spans from high-power EP applications[5] to low-amperage compact hall thrusters.[2] This makes them a promising candidate as an electron source in a low-current AF-MPD thruster. However, they have rarely been employed in a thruster as an on-axis cathode and at magnetic field strengths greater than 250 mT. Therefore, there is a need to analyse the behaviour and performance of a thermionic emission hollow cathode when subjected to axial magnetic field strengths far greater than those found in its typical applications.

The main requirement of the experimental setup presented here is to enable the parametric study and characterisation of heaterless hollow cathodes when subjected to an axial magnetic field. This is achieved by simultaneously measuring as many pertaining experimental parameters as possible, such as voltages, currents, temperatures and plasma parameters. Analysing the magnetic field strength and location's impact on these will allow to draw conclusions on the performance of the cathode.

1.1 Hollow Cathodes

Figure 1 depicts the general layout of a thermionic emission hollow cathode and its main components.

DOI: 10.13009/EUCASS2023-535

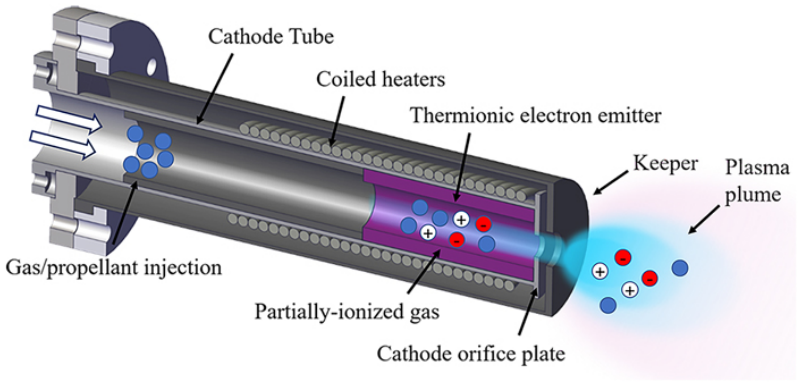

Figure 1: A schematic of a hollow cathode showing its basic components, including the emitter, keeper and plasma plume. Adapted from Goebel et al.[4]

The emitter is the electron source of the cathode. It makes use of thermionic emission, where a material emits electrons when heated. The effect is described by the Richardson-Dushman equation:

$$J = AT^2 e^{-e\phi/kT}, \tag{1}$$

where J is the current, A is a dimensionless constant, T is the absolute temperature, e is the charge, k is the Boltzmann constant and ϕ is the work function of the emitter material. A material with a low work function ϕ is desirable to maximise emission. The electrons emitted ionise the propellant flowing into the cathode and generate the plasma. The orifice provides the aperture needed in order to increase the gas and plasma pressure within the tube. The heater is used to pre-heat the emitter on start-up prior to ignition. Once ignited, the cathode is self-heating. The keeper electrode protects the cathode and heater from ion bombardment, helps to maintain the cathode temperature and facilitates turning on the cathode discharge.

1.2 Heaterless Hollow Cathodes

Heaterless hollow cathodes (HHCs) represent a subclass of hollow cathodes. As the name suggests, an HHC differs from an HC by disposing of the heater coil and relying on the current flow to heat up the emitter. This means that there is no need for an additional power supply for the heater coils, potentially saving on the total required PPU (Power Processing Unit) mass. The heating process is generally faster than with a heating element.[3,10] Without a heater, the cathode is less prone to thermal fatigue and is thus expected to have a longer lifetime.[12] These advantages make it an attractive option for in-space applications and a low-power AF-MPDT. Challenges are that the technology has never been flown in space, usually requires high voltages and that the plasma heats up other parts of the cathode alongside the emitter.

The entire ignition process of an HHC can be divided into three phases:[7,15] the initial breakdown, the heating phase and steady-state operation.

For the **initial breakdown**, a high voltage pulse between the emitter and the keeper breaks down the injected propellant gas. This occurs when the voltage is high enough to cause an ionisation avalanche. Generally, that breakdown voltage V_{br} decreases when the mass flow rate and thus internal cathode pressure p increases. The inner electrode gap (the distance between keeper and emitter) d also influences V_{br}.

During the **heating phase**, the emitter-keeper current heats up the emitter. Two types of plasma discharge regimes can be employed for this: a glow discharge, with a few hundred volts and a low mA-level current or an arc discharge with tens of volts and several to tens of amperes. When the emitter is hot enough to emit the desired current density, the main discharge voltage between the emitter and anode can be applied, and a transition to the main discharge/**steady state operation** occurs.

2. Experimental Setup Overview

A schematic overview of the setup that was designed is shown in fig. 2. With it, hollow cathodes can be tested in either a “diode”/stand-alone mode (plasma discharge only sustained between the emitter and keeper) or in a “triode” mode using an anode to simulate a thruster. All components are mounted on a removable grounded breadboard and are electrically insulated using alumina ceramic plating where required. Aluminium extrusion pieces are used as guide

DOI: 10.13009/EUCASS2023-535

rails on which the anode and cathode are mounted. This allows for variation of the distance between the cathode and anode d_{c-a}, as well as between the magnet and cathode d_{m-a}. Control and monitoring is achieved using LabVIEW.

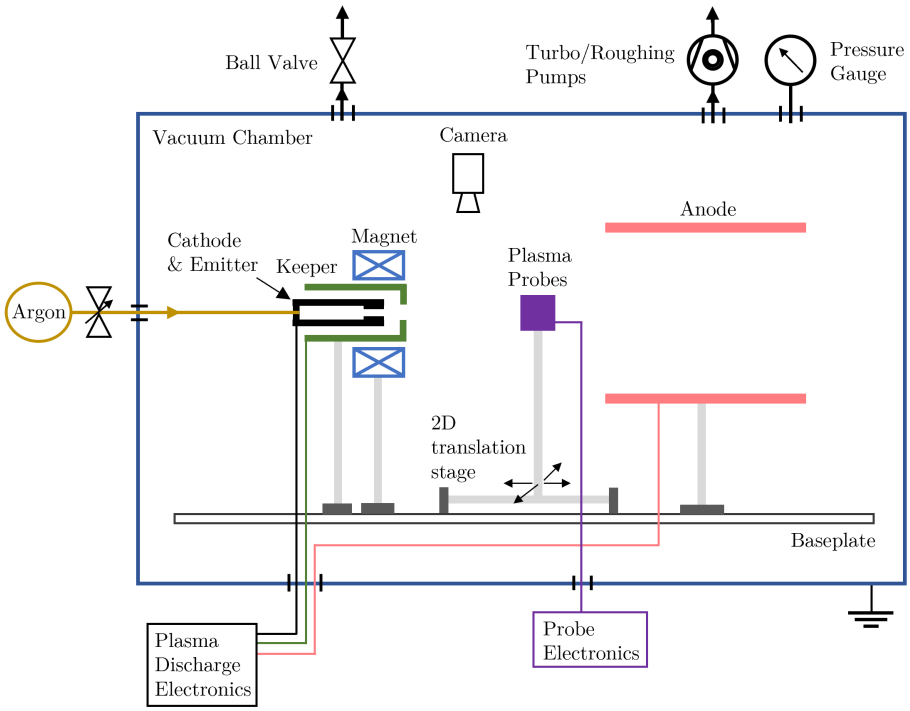

Figure 2: A simplified schematic of the Kākāpō experimental system, showing the main pressure and electrical connections for the cathode emission and measurement system.

2.1 Vacuum and Propellant System

The apparatus has been constructed at the National Satellite Test Facility of the Te Pūnaha Ātea Space Institute in Auckland within a 1 meter long x 0.8 m diameter cylindrical steel chamber. An Agilent TwissTorr 304FS turbomolecular pump in combination with an Edwards 18 dual-stage rotary pump is able to provide a base pressure of 10^{-6} Torr, which is monitored using an Agilent FRG-700 full-range Pirani inverted magnetron pressure gauge. The turbopump and pressure gauge are controlled with the same Agilent rack controller, which itself can be controlled and monitored from a PC via an RS-232 serial communication connection. A ball valve is used to vent the chamber. One end of the chamber is on hinges and can be fully opened for access. A KF-40 mounted viewport is installed for optical access.

Argon propellant which is 99.999 % pure is provided to the cathode via a 1/8-inch compression fitting propellant line system. An Alicat mass flow controller regulates the flow rate within the range of 0 to 100 sccm, with an accuracy of ±0.6 %. An additional needle valve is installed between the MFC and chamber feedthrough. A typical cathode operation mass flow of 10 sccm results in a background pressure of $\sim 10^{-4}$ Torr.

2.2 Plasma Discharge System

A detailed electrical schematic diagram of the cathode plasma discharge system is shown in fig. 3. The keeper power supply can reach 1000 V at a current of 2 A and has a maximum power draw of 2 kW. The emission power supply is rated for a voltage of 100 V at currents up to 40 A. Both PSUs are remotely controlled via LabVIEW. A variable 110 Ω potentiometer with a current rating of 2 A is connected in series with the keeper PSU and acts as a ballast resistor to limit the current and prevent arcing when the cathode is ignited.

The keeper current I_K is measured using a Tamura L18P005D15 open loop Hall effect current sensor that outputs a voltage in proportion to the current it is subjected to. It is rated for a current of 5A and has a measurement bandwidth of 100 kHz. A Riedon SSA-100 shunt current sensor with a differential voltage output is used to measure the emission current I_E at a bandwidth of 300 kHz. Both sensors' output voltages are recorded simultaneously using a MC USB-1808X DAQ device at a sample rate of 200 kHz per channel. Communication with the DAQ and transformation of the voltage data to current is done through LabVIEW. A high bandwidth was chosen for both the sensors and data

DOI: 10.13009/EUCASS2023-535

acquisition in order to allow for the measurement of possible oscillations or other fluctuations occurring on small timescales.

The keeper voltage V_K and anode voltage V_A are both measured with 10:1 attenuated passive voltage probes (Testec, 2.5 kV, 300 MHz Bandwidth) connected to a Rohde&Schwarz RTB2000 Oscilloscope with 100 MHz of bandwidth and a 2.5 GSa/s sampling rate. The recorded voltage data is transferred and saved using LabVIEW via USB.

The sensors and probes are all installed within an enclosed metal box and mounted on a grounded 9-inch rack together with the oscilloscope and power supplies. A 4-pin electrical feedthrough rated for up to 50 A per pin on a KF40 flange passes the power into the chamber. Initial ignition tests demonstrated the presence of electromagnetic interference that caused the failure of the sensors and DAQ. Subsequently, all sensor wires are shielded and grounded using copper mesh and run through ferrite cores. Shielded USB cables are used for data transfer.

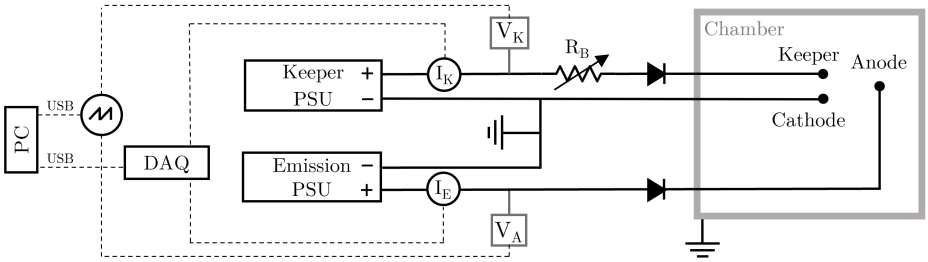

Figure 3: A wiring diagram of the plasma discharge system and instrumentation, showing the components within and outside the test chamber.

2.3 Other Diagnostics

The small KF-40 viewport, in combination with a mirror placed on the longitudinal axis of the cathode, enables optical access facing the keeper. However, for imagery from any other angles and in particular, perpendicular to the cathode, a camera within the chamber is required. To achieve this, a USB camera module with a 1920 x 1080 pixels resolution is installed inside a grounded aluminium box with a glass-covered circular cut-out. The camera is mounted on an aluminium rail that runs along the length of the chamber and can be placed at different distances from the cathode. A 9-pin D-sub feedthrough is used to transfer both power and image data.

A type N sheathed thermocouple with a 1.5 mm probe diameter is fixed to the keeper to measure the keeper temperature. PTFE-insulated Type K thermocouples measure the anode and magnet temperature. A sheathed type C T/C will be used to measure at higher temperatures of up to 2000°C within the cathode. A Pico TC-08 thermocouple data logger monitors and stores all temperature data.

Magnetic field strength measurements are conducted using the Lakeshore F71 Teslameter and a 1-axis Hall probe.

3. Magnet System

A crucial part of the apparatus is the magnet. Initially, a few critical requirements for the magnet and its field were identified. A maximum magnetic field strength of 0.6 T on-axis with an inner diameter (ID) of at least 50 mm is required to provide sufficient space for the cathode.

In a trade-off study, different options were considered. Both permanent magnet rings, as well as different cylindrical array configurations made up of permanent magnet bars magnetised along the axis parallel to the cylinder, were reviewed. While these arrays are able to create field lines similar in shape to those of a ring magnet or coil, magnetic field simulations demonstrated that even with the strongest grade of Neodymium magnets (N54), sufficiently high field strengths could not be reached for the desired ID. Superconducting electromagnets were eliminated due to the significant added complexity and cost, leaving an electromagnet as the only feasible option.

Different implementations of cooling the electromagnet were also assessed. This is particularly crucial for the application in-vacuum, where heat transfer is limited to radiation and conduction. Using hollow conductors for the coil winding and flowing water through them is an effective way of cooling. However, for the required field strength and the resulting number of coil turns, either multiple cooling stages or high-pressure water would be required. An

DOI: 10.13009/EUCASS2023-535

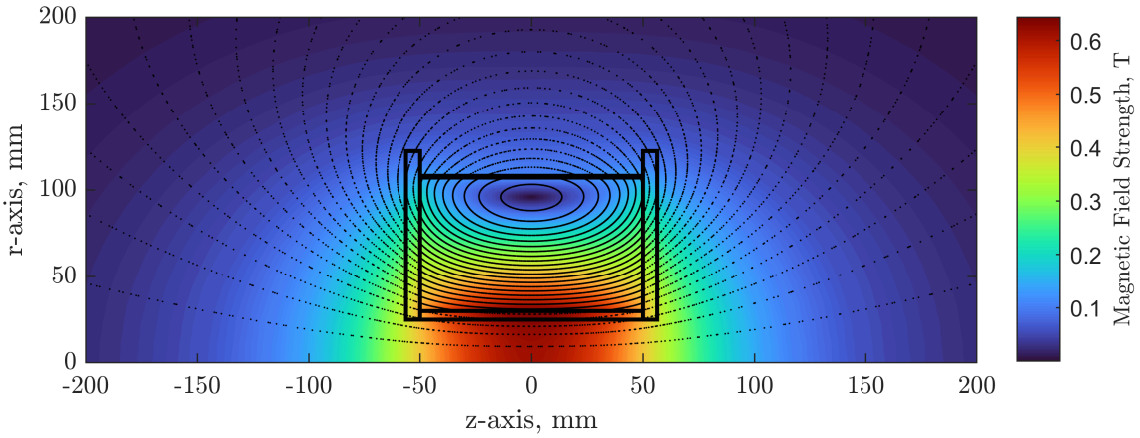

Figure 4: Contour plot of the simulated magnetic field strength around the coil at 32 A, including resulting field lines. An outline of the coil bobbin is also shown.

alternative water cooling option is to run tubes on the inner or outer diameter of the coil. The decision was made to employ a passive cooling system as it significantly reduces the complexity of the system design and is less prone to failure. A coil was designed that can be run at a specific duty cycle for a required duration before overheating and is cooled via conductive heat transfer. Square copper wires are used to maximise the contact area between the wires and thermal conduction within the coil.

The final coil design was derived via a parametric study. A detailed list of hard and soft requirements served as an input. The hard requirements were a maximum magnetic field strength of 0.6 T, min. ID of 50 mm, a maximum current draw of 32 A (limited by available PSU and feedthrough) and a run-time of at least 60 seconds at maximum field strength. The soft requirements were a coil mass below 25 kg and a length between 8 and 12 cm. An analytical magnet study yielded the parametric space for combinations of a number of turns N (both turns per layer and the number of layers), coil length L, conductor size and current I that resulted in a coil that met the requirements. The resulting coil mass, current and resistance were then used for a simple thermal model that calculated the increase in temperature of the coil over time, taking into consideration the increase of resistance with temperature as well as radiation. From these combinations, a final set of parameters was chosen.

In order to estimate the cool-down time of the coil, a full time-dependent 2D thermal heat transfer model was implemented in COMSOL. The model includes both the insulator and epoxy filler materials with which the gaps between the coils are filled. It also models the conductive path along the coil mount and additional copper heat pipes to the chamber walls.

Table 1 lists the final resulting coil properties.

Table 1: Final Coil Characteristics

Property	**Value**
Inner Diameter	60 mm
Outer Diameter	215 mm
Conductor	14 AWG square wire (1.768 mm side lengths)
Conductor Layers	44
Turns per Layer	57
Total Turns	2508
Total Conductor Length	1065 m
Coil Resistance (T = 300 K)	7.3 Ω
Magnetic Field Strength @ 32 A	612 mT

The coil is wound onto a 5 mm thick aluminium bobbin, resulting in an effective inner diameter of 50 mm and a total length of 112 mm. Duralco-4460 epoxy is used to bind the coil. This epoxy has good outgassing characteristics and is rated for temperatures up to 330 °C.[1] The copper wire enamel is rated for temperatures up to 200°C. It is this temperature that limits the maximum temperature of the coil and dictates the run time of the system. At a current of

DOI: 10.13009/EUCASS2023-535

32 A, this limit is 129 s. A bracket was designed and machined that attaches to the bobbin, securely mounts it onto the breadboard, and aids in heat transfer.

The magnet is powered by a 12 kW PSU capable of 32 A of current output. A surface plot of the simulated resulting magnetic field at 32 A of current is shown in fig. 4. A plot of the associated field strength along the coil axis is shown in fig. 5 together with measured data. The simulated magnetic field and measurements are in good agreement.

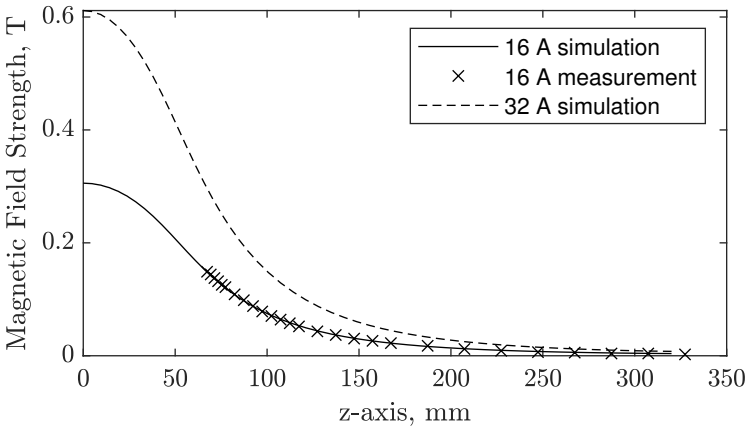

Figure 5: The simulated magnetic field strength along the magnet centre axis z for coil currents of 16 A and 32 A. Measurements taken with a hall probe for a current of 16 A are also shown.

4. Plasma Diagnostics

Quantifying the different parameters across the cathode plasma plume is an important step in understanding the magnetic field's impact on its performance. In Kākāpō, both Langmuir Probes (LPs) as well as a Retarding Field Energy Analyser (RFEA) mounted on a 2-axis translation system are to be used.

4.1 Plasma Probes

A Langmuir probe can be used to determine the plasma's electric potential V_p, electron temperature T_e and electron density n_e. The ion saturation current I_{sat} is another measurable plasma property and is often used as an indicator of the plasma ion density. In its most basic form, the LP is a conducting wire that is inserted into the plasma. The physical plasma parameters are derived by measuring the current flowing between the probe tip and the plasma I_p as a function of the externally applied probe bias voltage V_b. The resulting current-voltage (I-V) sweep of the LP is then post-processed to obtain the parametric values. The circuitry that was implemented to achieve this is shown in fig. 6.

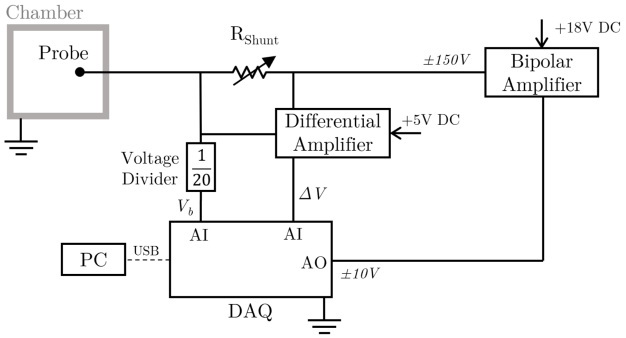

Figure 6: Electrical diagram of the Langmuir probe circuit used in this work.

An NI USB-6356 DAQ is used to output a ±10 V analogue signal (AO), which is amplified to ± 150 V by a bipolar amplifier and applied to the probe. The voltage drop ΔV across a variable resistor R_{Shunt} is amplified by a differential amplifier and measured with the DAQ (AI2) to determine the probe current $I_p = \Delta V / R_{Shunt}$. The probe bias

DOI: 10.13009/EUCASS2023-535

voltage V_b is directly measured (AI1) using a voltage divider to be within the input voltage limits of the device. The DAQ has a sampling rate of 100 kHz and simultaneously reads the inputs and writes the outputs. All wired connections outside of the chamber are made using shielded BNC cables to reduce noise.

For the utilisation of Langmuir probes in the presence of magnetised plasma, the circular motion of the ions and electrons along the magnetic field lines as a result of their interaction with them needs to be considered. The size of the ion and electron gyroradius is given by

$$r_{i/e} = \frac{mv}{qB} \quad , \tag{2}$$

where m is the particle mass, v is its velocity component perpendicular to the magnetic field direction, q is the particle's electric charge, and B is the magnetic field strength. Due to its larger mass, the ion gyro radius is always larger than the electron gyro radius.

If the probe radius r_p is smaller than the gyro radius of both ions and electrons, the IV characteristic remains unaffected. For $r_e < r_p < r_i$, only the electron collection is assumed to be affected. A common approach is thus to treat the ions as unmagnetised and only use the ion part of the IV curve for voltages around the floating potential and below to extract the plasma parameters.[13,14] At the highest expected field strength of 0.6 T in this setup, the ion radius can be estimated to be approximately 0.27 mm. Probe tips can be made of wires as thin as 50 µm and the magnetic field strength rapidly decreases with distance, meaning that the requirement can be fulfilled. Disregarding the size of the gyro radii, the effective probe surface is assumed to be a projection of the surface perpendicular to the magnetic field lines.[9] Therefore, a cylindrical probe tip has been chosen that is positioned within the symmetrical plane of the magnetic field. This way, perpendicularity to the magnetic field lines at any position is ensured, and the effective current collection area remains constant.

A custom Langmuir probe assembly has been designed in-house that can be easily mounted onto the 2-axis translation stage. A primary design requirement was the easy replaceability of the probe tip to allow for variation in the diameter and length of the probe exposed to the plasma. Figure 7 shows the schematic of the probe assembly with an example 127 µm probe wire diameter and 3 mm length. The entire probe tip can be unscrewed from the holder.

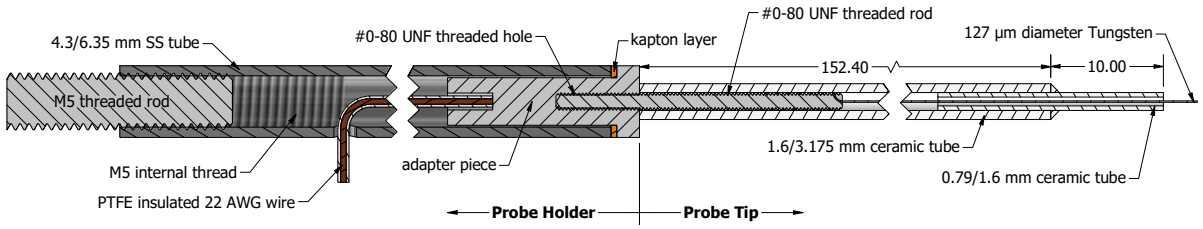

Figure 7: Schematic of the in-house design of the Langmuir probe assembly consisting of a probe holder and an interchangeable probe tip.

A second probe holder was built in a similar manner with an L-shaped steel tube to allow for scanning of the interior of the cylindrical anode.

An RFEA probe consists of an aperture in front of a stack of biased grids and acts as a directional energy filter. In Kākāpō, an RFEA will be used in ion collection mode to measure the full ion energy distribution function (IEDF) in the plasma plume. Due to the directional nature of the ion current sensed with such a probe, the presence of an ion beam can be demonstrated, and its extent measured. This will be of particular interest when the magnetic field strength is varied. The RFEA probe and circuitry are currently still under development.

4.2 Two-Axis Translation Stage

In order to remotely move the probes to different points in the plume and generate maps of the plasma parameters without having to open the chamber, an in-house probe positioning system has been designed and built in conjunction with the probes themselves. While vacuum-rated linear stages are commercially available, they are typically laid out for significantly higher loads than what is required here and come at a corresponding price point. For the sake of having a pre-determined constant orientation of the probe with respect to the cathode, which is of particular importance for the directional RFEA probe, a 2-axis linear translation stage design was chosen over a more straightforward combination of a linear and rotational stage. A stage size of at least 150 mm radially in each direction and 300 mm along the cathode axis was required.

DOI: 10.13009/EUCASS2023-535

The final stage design is shown in fig. 8. It consists of a 300 mm linear stage mounted on top of and perpendicular to a 400 mm linear stage and an additional 400 mm long guide rail. Each linear stage is made up of a stepper motor that is coupled to a high-precision M10 lead screw. As the screw is rotated, it moves a platform with a lead screw nut that is held in place by two 8 mm wide guiding rails along its length. All materials used are rated for use in a high vacuum application, including different lubricant-free linear and rotational bearings. All parts were designed and machined to a tight tolerance of 0.01 mm. Two NEMA 17 stepper motors with a holding torque of 0.6 Nm and a step angle of 1.8° are used to drive the lead screws.

The stage can cover an area of 380 x 285 mm with a minimum step size of 0.01 mm in both axes and at a maximum speed of 18 mm/s. The positional uncertainty is estimated to be ±0.15 mm. Both stepper motors are driven using Pololu Tic T500 stepper motor controllers, which receive commands via USB. The complete translation system is implemented in LabVIEW. The probe assembly can be directly screwed into the moving platform and positioned between the anode and cathode, within the anode and behind the anode if required.

5. First Cathode Ignition Tests

An image of the fully assembled chamber side of the setup is shown in fig. 8.

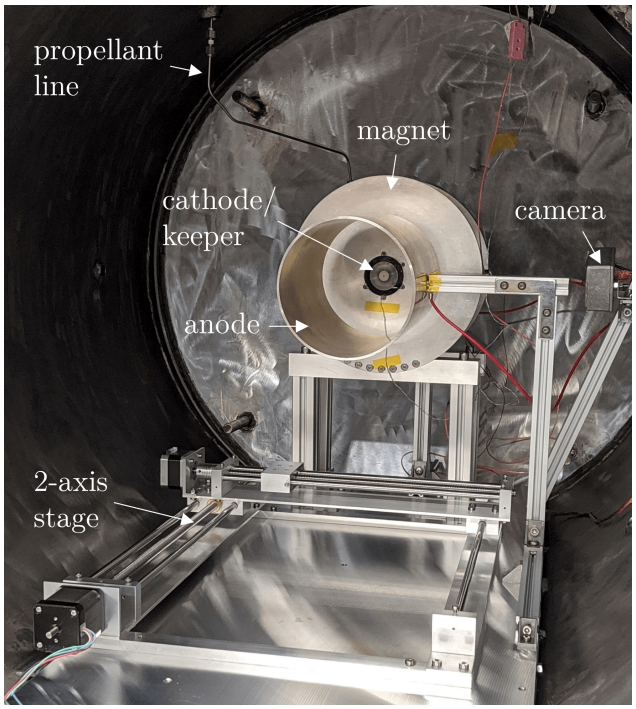

Figure 8: A picture of the full setup within the chamber and its main components.

First cathode discharge tests without an applied magnetic field have been conducted to ensure the correct functionality of the setup. A commercially available Kaufman & Robinson emitter insert was used for this purpose. It is tested in conjunction with a 150 mm wide cylinder anode placed at a distance of 50 mm from the keeper orifice. A typical discharge IV-characteristic is shown in fig. 9.

To ignite the cathode, a mass flow of 75 sccm is established and the keeper PSU voltage is ramped up. At this mass flow, breakdown occurs at around 370 V and current starts flowing from the keeper to the cathode tube through the plasma. The mass flow can then be lowered to 10 sccm, and a keeper current of 1.5 A is maintained with a keeper voltage of around 20 V. The anode PSU is subsequently turned on, and the voltage is increased. At around 55 V, the transition to the main anode discharge occurs (see fig. 10 for an image of the resulting plume). After this transition, a further decrease in anode voltage can be observed as the emitter heats up and its current density increases. Once the anode discharge is established, the keeper PSU can be turned off and left to float (in this case, it does this at approximately 10 V). For longer running tests, the keeper temperature reached a steady state of 590°C after 25 minutes.

DOI: 10.13009/EUCASS2023-535

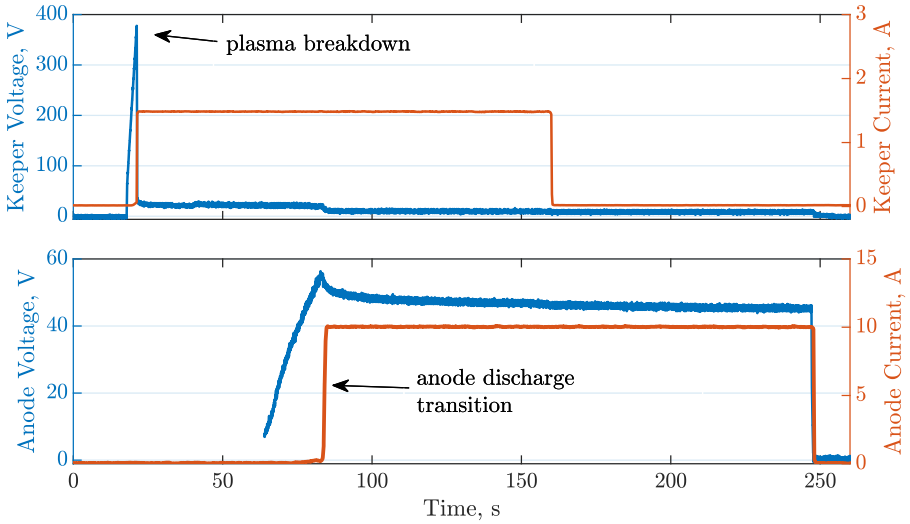

Figure 9: Recorded keeper and anode current and voltage curves for a full anode discharge test.

Figure 10: An image of the plasma plume between the cathode and anode at I_A=10 A.

6. Conclusions

With the Kākāpō facility, a test apparatus enabling the experimental study of heaterless hollow cathodes at applied axial magnetic fields was designed and commissioned from the ground up. Various instrumentation and diagnostic devices have been implemented to capture and quantify as many aspects of the process as possible. Complete control over these devices and recording of pertinent data is implemented through LabVIEW, allowing for remote operation. The basic operation of the setup has been demonstrated through a heaterless hollow cathode plasma discharge in conjunction with an anode.

A first experimental campaign involving a parametric study using a commercial HC to quantify the impact of different parameters on its operation will be conducted. From there, scaling laws will be derived for the cathode performance in dependence on the magnetic field strength. Experimental results will also be used to validate simulation data. This will allow to design and test a novel hollow cathode optimised for usage at high applied magnetic fields. Furthermore, the impact of the magnetic field strength on the erosion and degradation of the cathode will be analysed. The overall results of the experimental campaign performed with the setup are expected to establish the feasibility of applying a heaterless hollow cathode in a low-power HTS-AF-MPD thruster for future space missions.

DOI: 10.13009/EUCASS2023-535

7. Acknowledgments

This work is funded by the New Zealand Ministry of Business, Innovation and Employment (project title: "High Magnetic Field Electric Propulsion for Space", contract number RTVU2003).

References

[1] 600F-DURALCO 4460 Datasheet. Technical report, Cotronics Corp. https://www.cotronics.com/vo/cotr/pdf/4460.pdf (accessed July 2023).

[2] Giulia Becatti, Ryan W. Conversano, and Dan M. Goebel. Demonstration of 25,000 ignitions on a proto-flight compact heaterless lanthanum hexaboride hollow cathode. *Acta Astronautica*, 178:181–191, January 2021.

[3] Dan M. Goebel. Hollow cathode ignition studies and model development. In *29th International Electric Propulsion Conference*, Princeton, NJ, October 2005.

[4] Dan M. Goebel, Giulia Becatti, Ioannis G. Mikellides, and Alejandro Lopez Ortega. Plasma hollow cathodes. *Journal of Applied Physics*, 130(5):050902, August 2021.

[5] Dan M. Goebel and Emily Chu. High-Current Lanthanum Hexaboride Hollow Cathode for High-Power Hall Thrusters. *Journal of Propulsion and Power*, 30(1):35–40, January 2014.

[6] Hayato Kasuga, Jeohun Jeong, Keisuke Mizutani, Akira Iwakawa, Akihiro Sasoh, Kohei Kojima, Tatsuya Kimura, Yoshihiro Kawamata, and Masaaki Yasui. Operation Characteristics of Applied-Field Magnetoplasmadynamics Thruster Using Hollow Cathode. *Transactions of the Japan Society for Aeronautical and Space Sciences, Aerospace Technology Japan*, 16(1):69–74, 2018.

[7] Dan R. Lev, Gal Alon, Sagi Fisher, and Leonid Appel. Cathode Test Facility at Rafael. In *Space Propulsion 2016*, page 6, Rome, Italy, May 2016.

[8] Dan R. Lev, Ioannis G. Mikellides, Daniela Pedrini, Dan M. Goebel, Benjamin A. Jorns, and Michael S. McDonald. Recent progress in research and development of hollow cathodes for electric propulsion. *Reviews of Modern Plasma Physics*, 3(1):6, December 2019.

[9] Robert B. Lobbia and Brian E. Beal. Recommended Practice for Use of Langmuir Probes in Electric Propulsion Testing. *Journal of Propulsion and Power*, 33(3):566–581, May 2017.

[10] Pavel M. Puchkov. The low-current cathode for a small power electric propulsion. In *7th European Conference for Aeronautics and Space Sciences, Milan, Italy*, pages 3–6, 2017.

[11] Vincent K. Rawlin and Eugene V. Pawlik. A mercury plasma-bridge neutralizer. In *6th Electric Propulsion and Plasmadynamics Conference*, International Electric Propulsion Conference. American Institute of Aeronautics and Astronautics, September 1967.

[12] Anita Sengupta. Destructive physical analysis of hollow cathodes from the deep space 1 flight spare ion engine 30,000 hr life test. In *29th International Electric Propulsion Conference*, Princeton, NJ, 2005. Pasadena, CA: Jet Propulsion Laboratory, National Aeronautics and Space Administration.

[13] Peter C. Stangeby and G.M. McCracken. Plasma boundary phenomena in tokamaks. *Nuclear Fusion*, 30(7):1225–1379, July 1990.

[14] J. A. Tagle, Peter C. Stangeby, and S. K. Erents. Errors in measuring electron temperatures using a single Langmuir probe in a magnetic field. *Plasma Physics and Controlled Fusion*, 29(3):297–301, March 1987.

[15] V. Vekselman, Ya. E. Krasik, S. Gleizer, V. Tz. Gurovich, A. Warshavsky, and L. Rabinovich. Characterization of a Heaterless Hollow Cathode. *Journal of Propulsion and Power*, 29(2):475–486, March 2013.